PHYSICAL REVIEW MATERIALS **9**, 055203 (2025)

Free-standing zirconia metasurfaces for microwave resonant polarization conversion

Dimitrios C. Zografopoulos,[1,2,*] Konstantinos Ntokos,[1] Georgios Nousios,[2] Guillaume de Calan,[3] Odysseas Tsilipakos,[4]
Walter Fuscaldo,[2] Angelos Xomalis,[5] Laszlo Pethö,[6] José Francisco Algorri,[7,8,9] Victor Dmitriev,[10]
Traianos V. Yioultsis,[1] and Emmanouil E. Kriezis[1]

[1] *School of Electrical and Computer Engineering, Aristotle University of Thessaloniki, GR-54124 Thessaloniki, Greece*
[2] *Consiglio Nazionale delle Ricerche, Istituto per la Microelettronica e Microsistemi, Via del fosso del cavaliere 100, 00133 Rome, Italy*
[3] *Nanoe Corporation, 6 Rue des Frênes, Ballainvilliers 91160, France*
[4] *Theoretical and Physical Chemistry Institute, National Hellenic Research Foundation, GR-11635 Athens, Greece*
[5] *Nanoelectronics and Photonics Group, Department of Electronic Systems, Norwegian University of Science and Technology, Trondheim 7034, Norway*
[6] *Laboratory for Mechanics of Materials and Nanostructures, Empa, Swiss Federal Laboratories for Materials Science and Technology, Feuerwerkerstrasse 39, 3602 Thun, Switzerland*
[7] *Photonics Engineering Group, University of Cantabria, 39005 Santander, Spain*
[8] *CIBER-bbn, Instituto de Salud Carlos III, 28029 Madrid, Spain*
[9] *Instituto de Investigación Sanitaria Valdecilla, 39011 Santander, Spain*
[10] *Electrical Engineering Department, Federal University of Pará, CEP 66075-900 Belém, Brazil*

(Received 5 December 2024; revised 29 April 2025; accepted 16 May 2025; published 28 May 2025)

A dielectric zirconia metasurface for resonant polarization conversion at microwave frequencies is theoretically and experimentally investigated. The metasurface is composed of a periodic array of square slotted rings interrupted by solid bridge sectors that provide interconnection and mechanical stability to the free-standing metasurface structure. Moreover, they selectively break the symmetry of the unit cell, thus allowing for polarization conversion based on both weakly and strongly resonant modes, the latter stemming from bound states in the continuum. The main findings of the theoretical analysis are corroborated through the experimental characterization of a metasurface sample fabricated by a recently introduced three-dimensional (3D) printing technique based on fused filament fabrication. Going beyond the target application of resonant polarization conversion, this work proposes an approach for the realization of high-permittivity, 3D-printed zirconia metasurfaces with submillimeter features for strong wave-matter interaction at microwave frequencies.

DOI: 10.1103/PhysRevMaterials.9.055203

I. INTRODUCTION

All-dielectric metasurfaces composed of high-permittivity resonators have attracted extensive scientific attention in recent years as they provide a compact, low-profile platform for intense light-matter interaction at the subwavelength level. They emerge as the enabling factor in numerous applications based on the manipulation of the amplitude, phase, polarization, or beamshape of free-space propagating waves [1,2]. Among such applications, multifunctional polarization manipulation has been demonstrated in dielectric metasurfaces for polarization rotation, beam splitting, or polarization-dependent lensing and holography [3].

Although in the infrared and optical spectrum the gamut of available transparent, high-permittivity materials is limited (including mostly III-V and group IV semiconductors), at microwave frequencies dielectric materials with relative permittivity values in the $\varepsilon_r = 10$–70 range and very low losses are available in the form of ceramics and their composites. Leveraging such high permittivity values, various resonant metasurfaces have been demonstrated based on physical mechanisms such as quasibound states in the continuum (qBIC) [4,5] or bright toroidal dipole modes [6–8]. The constituent ceramic resonators can be manually assembled and fixed on a substrate [9] or positioned inside a low-permittivity milled foam material [4] or a three-dimensional (3D) printed substrate [7].

However, the true potential of ceramic microwave metasurfaces can be unlocked by resorting to 3D-printing techniques of the metasurface as a whole, thus greatly improving the manufacturing speed, repeatability, and process flow. Several polymeric or nonpolymeric materials have been used in 3D-printed components for microwave applications [10,11]. Among these materials, zirconia stands out thanks to its high relative permittivity ($\varepsilon_r \simeq 30$) and moderately low losses ($\tan\delta \simeq 0.002$). To be used in 3D manufacturing, pure zirconia (ZrO_2) is partially stabilized in tetragonal form by usually adding yttrium oxide, providing a material with excellent mechanical properties, such as shock and bending resistance. By employing techniques like the nanoparticle jetting technique [12] or the recently proposed fused filament fabrication (FFF) technique [13], various zirconia-printed components have been demonstrated, such as a dielectric helical antenna

---

[*] Contact author: dzogra@ece.auth.gr

for radar cross-section reduction [14], or other types of dielectric resonator antennas [15,16].

In this work, we extend the paradigm to zirconia-based 3D-printed metasurfaces by investigating a free-standing, interconnected metasurface for resonant polarization conversion. The metasurface unit cell is characterized by a square slotted ring interrupted at two parts by zirconia bridges. We have recently shown that reduced-symmetry metasurfaces operating in the infrared support multiple strongly resonant qBIC modes [17,18] resulting from (i) the transformation of symmetry-protected BIC (SP-BIC) to qBIC resonant modes, or (ii) the geometrical tuning for the excitation of accidental BIC (A-BIC) modes.

In the proposed design, the presence of two bridges not only allows for qBIC mode excitation, but it also allows for resonant polarization conversion with a variable bandwidth, stemming from weakly or strongly resonant modes with quality factors (Q-factors) different by orders of magnitude. Moreover, the metasurface is free-standing and made of a single dielectric material (zirconia), which is 3D-printed by the FFF method. To the best of our knowledge, this is the first example of a 3D-printed all-zirconia microwave metasurface with submillimeter features, otherwise unattainable by mechanical processing of a zirconia slab. This 3D-printing technique has potential for wider applicability and it can significantly lower the fabrication cost of dielectric components for microwave applications.

The electromagnetic response of the metasurface is investigated theoretically, providing insight into the nature of the involved resonances, using a variety of tools: full-wave scattering simulations, eigenfrequency analysis, and multipole expansion, the latter to investigate the BIC nature of certain resonant modes. Interesting operation regimes are identified where the metasurface splits the impinging linearly polarized plane wave into four beams corresponding to reflectance/transmittance of the co/cross-polarization in almost equal proportions. The main results are corroborated through the characterization of a 3D-printed sample in an anechoic chamber.

II. THEORETICAL ANALYSIS

A. Layout and symmetry considerations

The layout of the investigated metasurface is shown in Fig. 1(a). The metasurface is composed of a square periodic lattice with a pitch of $p = 5$ mm. In each unit cell there is a square slotted ring interrupted at two sides by bridges of width $g = 1.5$ mm, as depicted in Fig. 1(b). The bridges ensure the continuity of the metasurface structure and its mechanical stability. The external width of the ring is $w = 4$ mm and the slot width is $s = 0.5$ mm. The metasurface is designed for fabrication by means of 3D-printing in a free-standing layer of zirconia whose thickness is $t = 2.15$ mm. Figure 1(c) shows a photo of the fabricated sample, which is composed of 20×20 unit cells for a total area of 10×10 cm^2. Details on the sample fabrication follow in Sec. III.

The metasurface is illuminated by a normally impinging x-polarized plane wave, as defined in Fig. 1(a). Apart from providing mechanical support, the presence of the two bridges strongly determines the electromagnetic response of the metasurface. In particular, the metasurface without bridges ($g = 0$) possesses C_{4v} symmetry in a 2D x-y description, which leads to all possible modes, except those with a dipolar radiation pattern, being dark [17]. The bridges break the symmetry of the unit cell, reducing it to C_s, leaving only one diagonal plane of symmetry and thus enabling the excitation of quasi-BIC resonances. Polarization conversion is provided when the polarization of the incident wave does not coincide with the diagonal axis of symmetry. In the reduced-symmetry structure, polarization degeneracy can exist, as will be shown, when the incident plane wave is linearly polarized along the x- or y-axis as defined in Fig. 1.

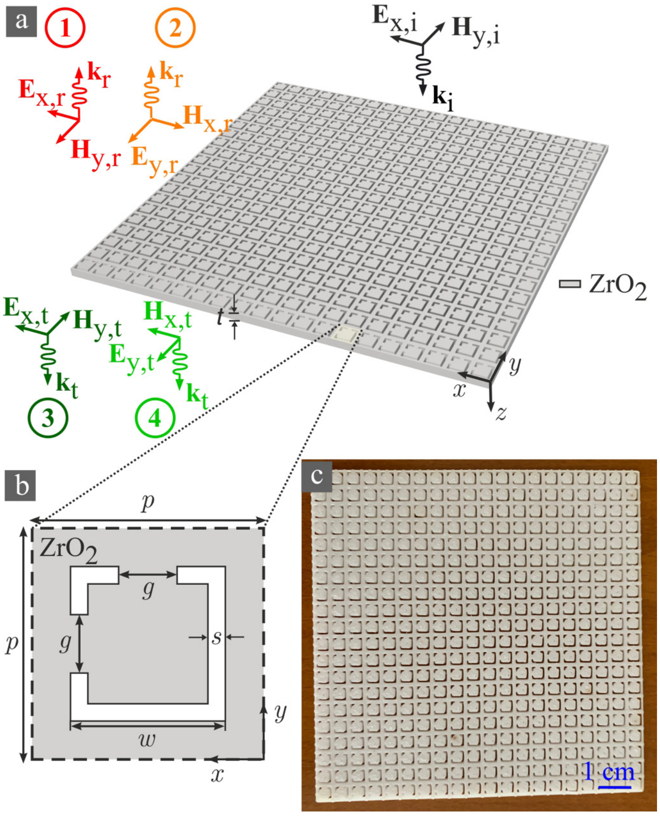

FIG. 1. (a) Bird's eye view of the investigated zirconia metasurface and definition of the incident, reflected, and transmitted linearly polarized plane waves. The metasurface is 3D-printed in a single free-standing zirconia slab. The yellow-shaded area denotes the unit cell of the periodic array. (b) Definition of the unit cell geometry ($p = 5$ mm, $w = 4$ mm, $g = 1.5$ mm, $s = 0.5$ mm, and $t = 2.15$ mm). (c) Photo of the fabricated sample composed of 20×20 unit cells for a total area of 10×10 cm^2.

To theoretically investigate the metasurface properties, we define four ports as in Fig. 1(a). Port 1 is used as the excitation port of an x-polarized impinging plane wave used in the full-wave simulations, Port 3 is the transmission port through the metasurface with reference to the x-polarization, and Ports 2 and 4 describe y-polarized reflection and transmission, respectively. Based on this definition and the symmetry properties of the metasurface, the complex S-parameters for the four ports are expressed as $S_{11} = S_{22} = r_{xx} = r_{yy} = r_{\parallel}$, $S_{21} = S_{12} = r_{xy} = r_{yx} = r_{\perp}$, $S_{31} = S_{42} = t_{xx} = t_{yy} = t_{\parallel}$, and $S_{41} =$

$S_{32} = t_{xy} = t_{yx} = t_{\perp}$, whereas the corresponding power coefficients describing the reflectance R and transmittance T at the four ports are $R_{\parallel} = |r_{\parallel}|^2$, $R_{\perp} = |r_{\perp}|^2$, $T_{\parallel} = |t_{\parallel}|^2$, and $T_{\perp} = |t_{\perp}|^2$. The absorptance of the metasurface due to losses in the dielectric material is calculated as $A = 1 - R_{\parallel} - R_{\perp} - T_{\parallel} - T_{\perp}$ or by integrating the power loss density in the zirconia volume; we have verified that the two approaches lead to identical results. Full details on the effect of the 3D symmetry properties of the metasurface on its scattering matrix are provided in Appendix A, where it is demonstrated, on the basis of symmetry considerations alone, that the metasurface response is indeed described by four independent scattering coefficients.

B. Full-wave simulation analysis

The electromagnetic properties of the metasurface are numerically investigated by means of the finite-element method implemented in the commercial software comsol multiphysics. Periodic conditions are applied at the xz and yz boundaries of the unit cell, and the four ports are defined at two z-planes placed 2 cm from the metasurface, i.e., at a distance above one wavelength for the lowest frequency under consideration. It is remarked that under the investigated conditions, the metasurface operates in a nondiffractive regime. The value for the relative permittivity of zirconia used in the theoretical analysis is $\varepsilon_r = 32.8$ and its loss tangent is $\tan\delta = 0.003$. This value resulted from the experimental characterization of a bulk zirconia sample measured inside a WR-90 waveguide as detailed in Appendix B. To study the effect of the material absorption losses, the analysis is performed initially considering a lossless material with $\tan\delta = 0$.

Figure 2(a) summarizes the simulation results by showing the reflectance, transmittance, and absorptance spectra, as previously defined. In the lossless case, 11 spectral features associated with resonant modes are identified, of which M7 exhibits a very sharp linewidth, as shown in the zoomed spectra of Fig. 2(b). Due to its very strongly resonant nature ($Q_{\mathrm{M7}} \simeq 5 \times 10^4$), this mode does not manifest when the material losses are added in the analysis, as a result of resonance quenching. The other resonant modes are significantly broader and they are observed in the spectra calculated for both the lossy and lossless case. Their resonant frequencies coincide with the absorption peaks in the absorptance spectrum of Fig. 2(a).

An interesting property of the metasurface is that at certain frequencies the incident power is equally distributed among the four ports. These frequencies are marked with blue shaded dots in Fig. 2(a) for the lossless case. Such equal polarization beam splitting can be more or less resonant, with a bandwidth depending on the resonance linewidth. In the presence of losses, these cases of beam splitting are still observed, albeit without exactly equal power distribution due to the absorption losses in zirconia.

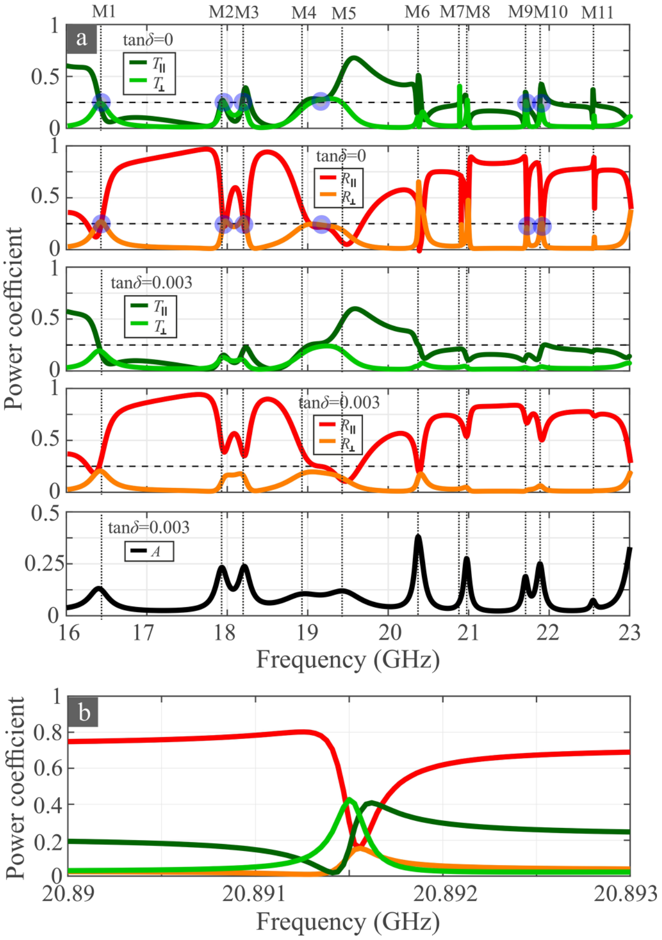

FIG. 2. Transmittance, reflectance, and absorptance spectra for the investigated metasurface. The dotted vertical lines indicate the resonant frequencies. The blue shaded dots indicate frequencies at which equal power splitting is achieved among the four ports.

C. Eigenfrequency analysis

Aiming to provide additional insight on the nature of the resonant modes, we conducted an eigenfrequency analysis on the dependence of the mode resonant frequencies f_r and Q-factors as a function of the bridge width g, which determines the level of asymmetry in the unit cell. Periodic boundary conditions were applied at the lateral walls of the metasurface unit cell, whereas at the top and bottom of the computational domain a perfectly matched layer backed by scattering boundary conditions was implemented. Eigenfrequency simulations were performed at the Γ point, corresponding to normally incident plane waves.

The results are presented in Figs. 3(a) and 3(b) for f_r and Q, respectively, calculated for the lossless case. The $R_{\perp}$ spectrum is added as a guide to the eye, as the resonant frequencies for $g = 1.5$ mm correspond to the maxima observed in the spectrum. At $g = 0$, namely for the symmetric square ring unit cell, six modes (M4–M6 and M9–M11) show diverging quality factors, which is an indication of SP-BIC modes [2,19]. Indeed, for the symmetric metasurface ($g = 0$) the corresponding profiles of the transverse resonant magnetic field shown in Fig. 4 exhibit symmetric patterns stemming from their SP-BIC nature, which inhibits coupling with the impinging plane wave and leads to a diverging radiative Q-factor. When the symmetry of the structure is reduced ($g = 1.5$ mm), so is the field profile, thus transforming the pure SP-BIC modes to quasi-BIC. Mode M9 shows more robustness to such

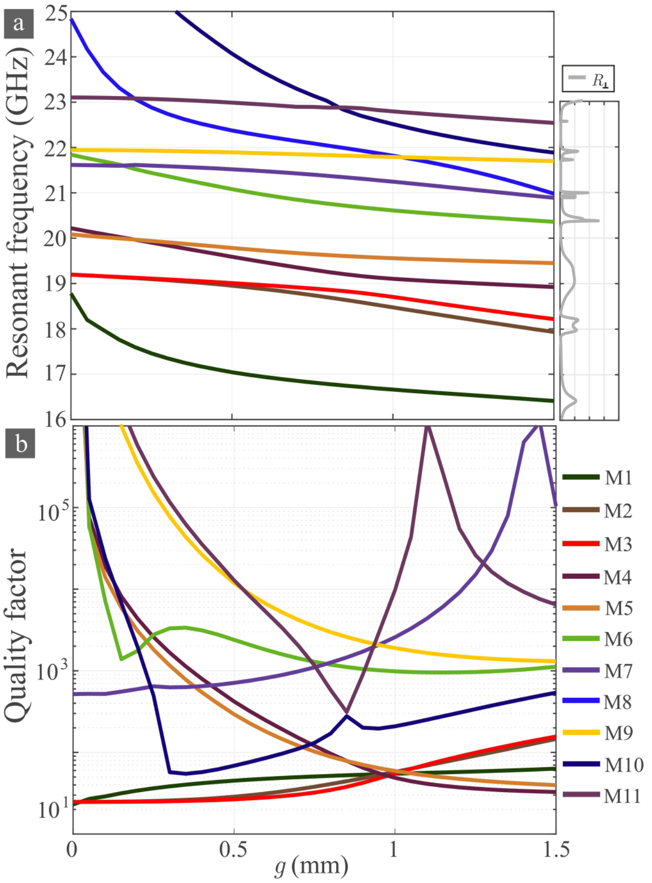

FIG. 3. (a) Resonant frequency and (b) quality factor of the 11 investigated resonant modes as a function of the bridge width g.

perturbation (cf. the field profile for $g = 1.5$ mm), which is reflected in its higher overall quality factors in Fig. 3(b) in the entire range of g values considered.

Apart from SP-BIC modes, the local maxima observed in Fig. 3(b) for $g \neq 0$ in the case of modes M7 and M11 correspond to A-BIC modes, where the high quality factors stem from the negligible coupling between the impinging plane wave and the field distribution at certain g values. The A-BIC condition mode M7 is satisfied for a value of g close to 1.5 mm, which explains the very high Q-factor observed in the spectra of Fig. 3(b). The quality factors for the rest of the bright modes at $g = 1.5$ mm range from several tens to hundreds in accordance with the linewidths observed in the spectra of Fig. 2. Therefore, the resonant regimes corresponding to strong polarization conversion and beam splitting stem from the rich physics of the metasurface that involve both strongly resonant SP-BIC/A-BIC modes and moderately resonant bright modes.

D. Multipole expansion analysis

To provide further evidence on the BIC nature of modes M4–M6 and M9–M11, we have performed a multipole expansion in the polarization current distributions of the eigenfields calculated as in Fig. 4 following the procedure presented in Ref. [20]. Figure 5 shows the results for modes M4 and M5, where in the calculation of the scattering magnitude of each multipole appropriate factors were taken into account to allow for a direct comparison among the different multipole moments [20]. In the symmetric case, M4 is characterized by a dominant magnetic quadrupole moment $Q_{xy}^{(m)}$, consistent with the corresponding magnetic field profile of Fig. 4. This moment does not radiate into the far-field, hence mode M4 is a symmetry-protected BIC. Mode M5 exhibits a dominant toroidal dipole T_z and to a lesser extent electric dipole p_z moments, as evidenced by the loops in the magnetic field profile in Fig. 4. Being both z-polarized, these two moments also do not radiate into the far field, thus confirming the BIC nature of mode M5 as well.

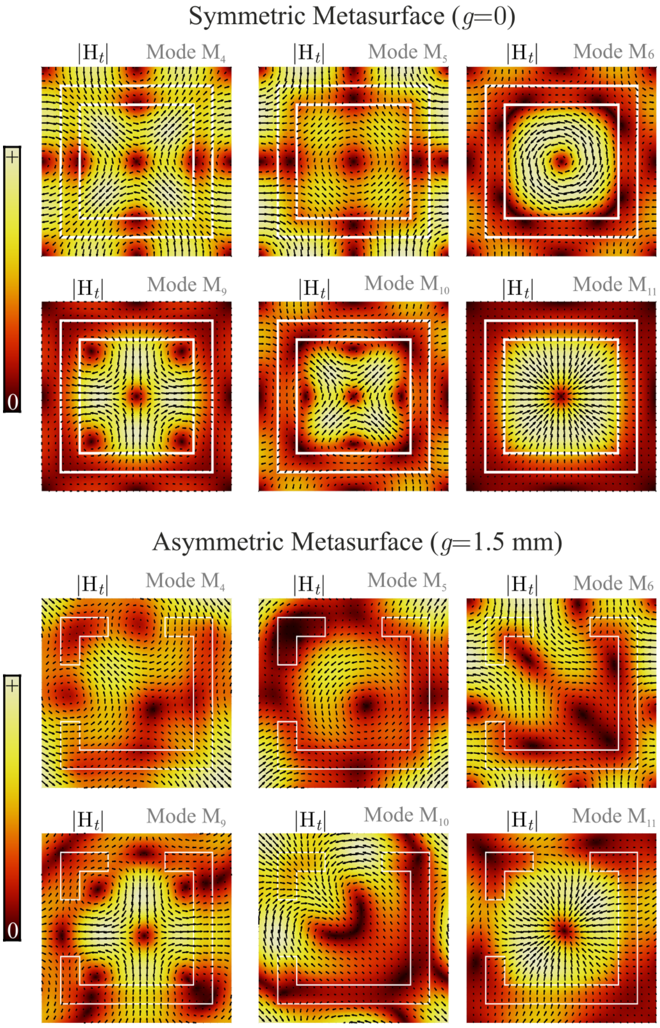

FIG. 4. Transverse magnetic-field profiles of modes M4–M6 and M9–M11 calculated at the midplane of the metasurface for the symmetric ($g = 0$) and asymmetric case ($g = 1.5$ mm).

When the symmetry of the metasurface is broken ($g = 1.5$ mm), so is the symmetry of the resonant mode profiles, which gives rise to additional multipole moments. In particular, for both cases of the investigated modes, symmetry breaking induces strong components of the in-plane magnetic moment m_x (m_y) and the quadrupole electric moment Q_{yz}^e (Q_{xz}^e), which can be directly coupled to a y- (x-) polarized impinging plane wave, respectively [20]. Therefore, the multipole analysis reveals the mechanism underlying the transition

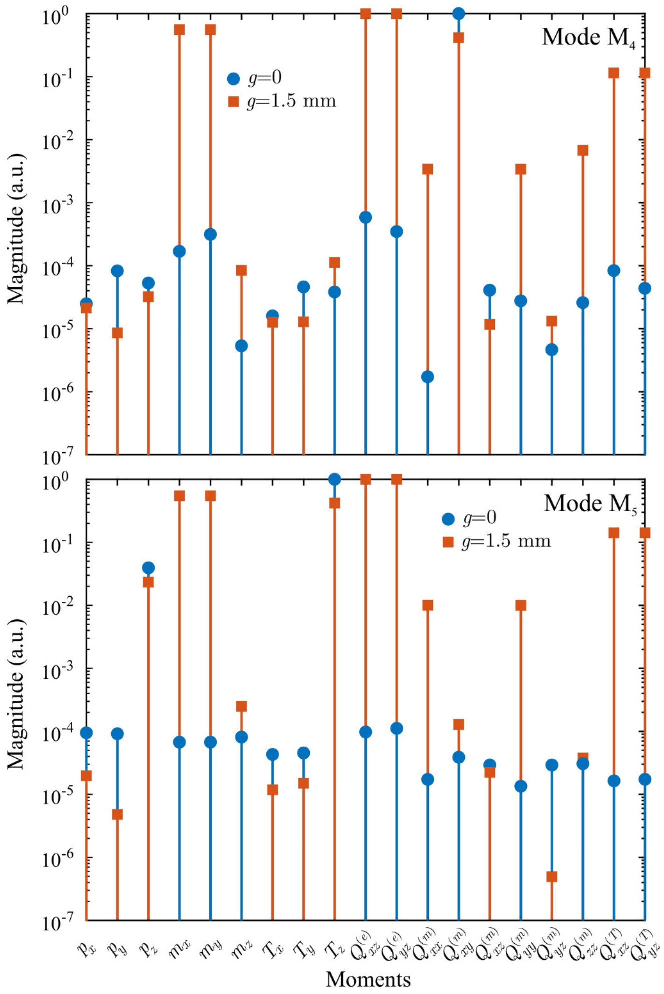

FIG. 5. Multipole expansion analysis for BIC modes M4 (top panel) and M5 (bottom panel) calculated in both the symmetric and asymmetric metasurface case.

from pure BIC to quasi-BIC resonances for modes M4 and M5. Similar conclusions hold also for the BIC modes M6 and M9–M11, as briefly discussed in Appendix C.

III. EXPERIMENTAL DEMONSTRATION

A. Additive manufacturing metasurface fabrication

The metasurface was fabricated by an additive manufacturing process compatible with ceramic materials, in particular an FFF-based 3D printing technique named Zetamix, recently introduced by Nanoe Corporation [13,21]. It allows for creating complex ceramic shapes in alumina, zirconia, and also steel. In this process, a ceramic/thermoplastic filament with very high loading of ceramic is printed with a standard printer by melting the filament through a deposition nozzle, and the part is produced layer by layer to form a 3D printed object, which is then debinded (by chemically removing the binder) and sintered (heat-treated at 1400°–1500°) to obtain the final dense ceramic part. The investigated free-standing metasurface is compatible with the FFF technique, as it is composed of an interconnected layer of zirconia material. The slot width $s = 0.5$ mm was the challenging factor in terms of fabrication, as this dimension is comparable with the nozzle size, and it demands careful compensation in the stage of the model design to properly account for the reduction of the zirconia volume during sintering.

It should be mentioned that there are a few other technologies applicable for the fabrication of parts similar to the investigated structure, mainly resin-based manufacturing [stereolithography (SLA) [22,23] or digital light processing (DLP) [3]] and nanoparticle jetting (NPJ) [12,24]. While both can in principle manufacture finer features, there would be some significant risk of failure in the case of NJP because of the very brittle nature of green parts, and some difficulty in cleaning the very fine channels with SLA/DLP. Importantly, the cost of such parts made with FFF is much more attractive and compatible with industrial applications than that of other candidate techniques.

The fabricated sample dimensions are 10×10 cm^2. Although printing larger samples was found to be possible, ensuring their uniformity over large areas becomes increasingly challenging. Assembling tiles is an option in case larger samples are needed. In terms of the fabrication speed, the printing time for the metasurface was two hours, while debinding and sintering took approximately two days. The debinding and sintering stage is known to be time-consuming, but since it is a batch process, hundreds of parts can be processed simultaneously if larger-scale production is targeted.

Furthermore, to adjust for the approximately 20% shrinkage during sintering, which is different along the xy and z directions, the recommended oversizing factor was applied in the slicer software. In addition, some optimization work on printing parameters was required to get the correct level of flatness on the printing surfaces. However, the lateral wall flatness inside the slotted regions was much harder to control, leading to deformations of the slot geometry. This factor is mostly accountable for the discrepancy observed between measured and theoretical results on the metasurface electromagnetic response.

B. Anechoic chamber measurements

The measurement setup is shown in Fig. 6(a). First, the metasurface sample is mounted on a lightweight plastic frame, which is subsequently attached to a square opening, cut on a slab made of radar absorbing material (RAM), in order to eliminate spurious diffraction effects. The frame is then positioned between a pair of transmitting (Tx) and receiving (Rx) K-band horn antennas (FLANN Microwave 20240) with a standard gain of 20 dBi, which are connected to a vector network analyzer (Anritsu 37397D). All measurements were conducted inside an anechoic chamber. Before conducting the measurements, a transmission (S_{21}) response calibration was performed without the metasurface sample. To measure the cross-polarization transmission coefficient $t_\perp$, the Rx antenna was rotated by 90 degrees. Reflection measurements were conducted using the same pair of antennas placed in a reflection configuration. The antennas were isolated by placing a slab of RAM between them, and the reflection response calibration was performed by placing a copper plate instead of the metasurface sample. Note that in all cases, the distances between the antennas and the sample were sufficiently larger

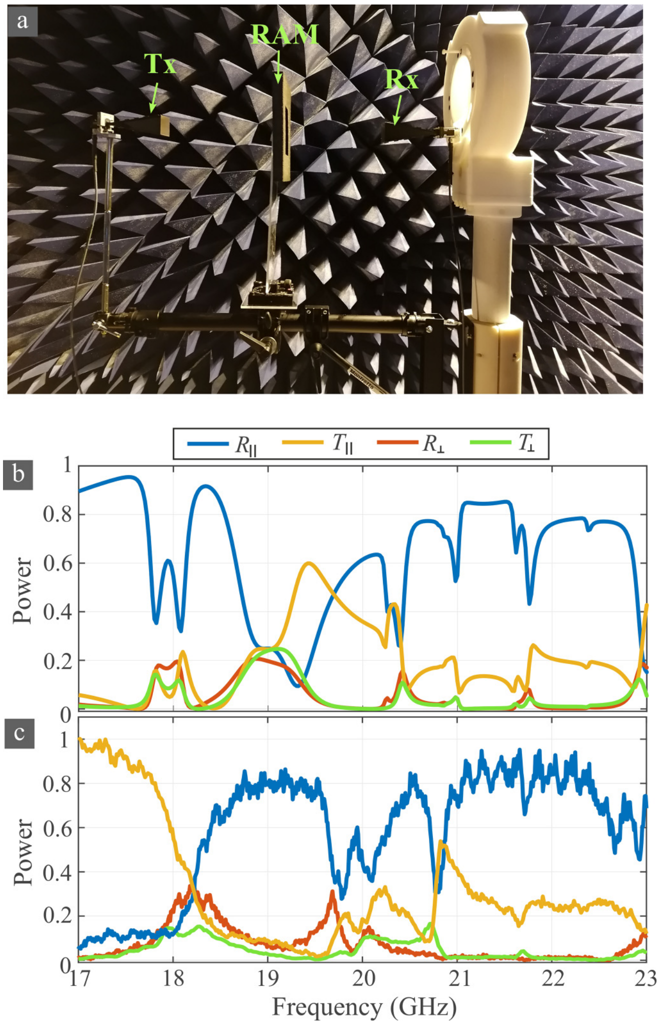

FIG. 6. (a) Photo of the anechoic chamber measurement setup, showing the transmit and receive antennas and the sample placed in a frame of RAM material on a placeholder for measurements in transmission mode. (b) Theoretically calculated and (c) experimentaly measured spectra for the power coefficients of co- and cross-polarizations in reflection and transmission.

than the near-field limit of the antennas. The measurements were recorded between 17 and 23 GHz with a spectral resolution of 15 MHz.

Figure 6(b) shows a comparison between the four experimentally measured and theoretically calculated power coefficients. Fair overall agreement is observed, especially for the cross-polarization coefficients $R_{\perp}$ and $T_{\perp}$. Overall, the observed level of discrepancy is attributed to the nonperfect uniformity of the metasurface features of the fabricated sample, as observed in Fig. 1(c). Such statistical variation of the unit cell dimensions can account for the quenching of strongly resonant modes, due to resonance broadening [18], and generally leads to non-negligible deviation of the electromagnetic response of the metasurface. However, this was to a certain extent expected, as one of the main goals of this work was to challenge the fabrication capabilities of the employed 3D-printing technique. This effect is expected to be largely alleviated in metasurfaces composed of features with relaxed dimension requirements. In addition, the observed discrepancy is also attributed to the finite (limited) metasurface extent, especially in the low-frequency end.

IV. CONCLUSIONS

To summarize, we have investigated an all-dielectric zirconia slotted metasurface designed to perform resonant polarization conversion in the microwave K-band. The linear polarization conversion is achieved by breaking the symmetry C_{4v} of the unit cell by two zirconia bridges and by properly selecting the polarization of the incident wave. The zirconia bridges interrupt the continuity of a square slot and also provide mechanical stability to the structure.

It is shown that polarization conversion occurs at resonant bands stemming from both bright and qBIC resonances, allowing for four-way beam splitting between the x- and y-linear polarizations and directions of propagation with almost equal efficiency. The theoretical findings are supported by a proof-of-concept experimental campaign involving a zirconia metasurface sample, fabricated by 3D-printing at the limits of current technology, and characterized via anechoic chamber measurements. Optimization of the 3D-printing process can reduce the observed inhomogeneity in the slotted areas of the metasurface, which was the main factor for the observed level of discrepancy between the measured and theoretically calculated scattering parameters of the sample.

The proposed metasurfaces can be used in microwave/millimeter wave systems where polarization beam splitting and control is needed, such as in wireless links or polarimetric radars and imaging, leveraging zirconia's favorable properties, such as durability, thermal stability, and chemical stability. Nevertheless, the proposed fabrication technique is general and can be applied for engineering a variety of components, e.g., dielectric antennas, reflectarrays, resonators, or metalenses.

ACKNOWLEDGMENTS

This work was supported by the Project No. PRIN-2022 ALPHA “ALl-dielectric resonant metasurfaces enhancing PHoton emission phenomenA” (CUP:D53D23001060006) funded by the Italian Ministry of University and Research. W.F. acknowledges the support of the Project No. ECS00000024 “Ecosistemi dell'Innovazione”-Rome Technopole of the Italian Ministry of University and Research, public call no. 3277, PNRR-Mission 4, Component 2, Investment 1.5, financed by the European Union, Next GenerationEU (CUP: B83C22002890005).

APPENDIX A: SCATTERING MATRIX ANALYSIS OF THE METASURFACE

The 3D symmetry group of the metasurface unit cell is C_{2v}. It contains the following elements of symmetry: the horizontal plane of symmetry σ_z (the midplane of the metasurface), the diagonal plane of symmetry σ_d (the $x = y$ plane with reference to Fig. 1), and the twofold rotational axis C_{2xy}, which is an intersection of the two planes of symmetry.

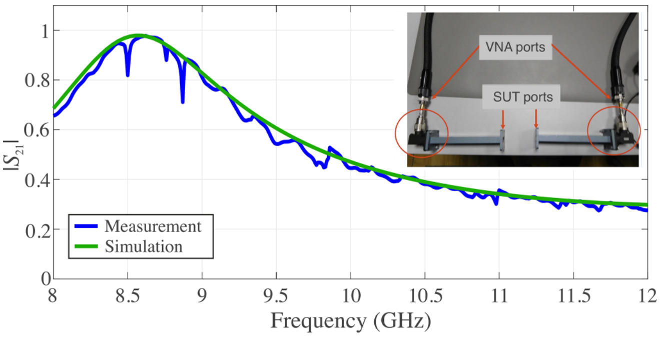

FIG. 7. Measured $|S_{21}|$ spectrum of the test zirconia slab in a WR-90 waveguide and best-fitted simulation result.

We analyze the metasurface as a four-port system, as defined in Fig. 1. The output $\mathbf{E}_{\text{out}}$ and input $\mathbf{E}_{\text{in}}$ waves are connected by the 4 × 4 scattering matrix $\bar{\mathbf{S}}$:

$$\mathbf{E}_{\text{out}} = \bar{\mathbf{S}}\mathbf{E}_{\text{in}}. \tag{A1}$$

This matrix must be invariant under any operation of the C_{2v} symmetry group. Mathematically, this condition can be written in terms of the commutation relations [25]:

$$\bar{\mathbf{R}}\bar{\mathbf{S}} = \bar{\mathbf{S}}\,\bar{\mathbf{R}}, \tag{A2}$$

where $\bar{\mathbf{R}}$ is the four-dimensional representation of a symmetry element. In our case, we can choose σ_z and σ_d. Using these elements and the condition of reciprocity$\bar{\mathbf{S}} = (\bar{\mathbf{S}})^t$, one arrives at the matrix

$$\bar{\mathbf{S}} = \begin{pmatrix} S_{11} & S_{12} & S_{13} & S_{14} \\ S_{12} & S_{11} & S_{14} & S_{13} \\ S_{13} & S_{14} & S_{11} & S_{12} \\ S_{14} & S_{13} & S_{12} & S_{11} \end{pmatrix}. \tag{A3}$$

The derivation of the scattering matrix is based only on the symmetry constraints, therefore its structure does not depend on frequency. The matrix has four independent complex parameters, which depend on the parameters and dimensions of the metasurface. In accordance with the field reflection and transmission definitions in Sec. II, it holds for the scattering matrix $\bar{\mathbf{S}}$: $S_{11} = S_{22} = S_{33} = S_{44} = r_{\parallel}$, $S_{12} = S_{21} = S_{34} = S_{43} = r_{\perp}$, $S_{24} = S_{42} = S_{31} = S_{13} = t_{\parallel}$, and $S_{23} = S_{32} = S_{41} = S_{14} = t_{\perp}$.

Interestingly, $\bar{\mathbf{S}}$ coincides with the scattering matrix of the waveguide directional coupler discussed in [26]. Using the unitary condition assuming a structure without losses,

$$\bar{\mathbf{S}}(\bar{\mathbf{S}}^*)^t = \bar{\mathbf{I}}_4, \tag{A4}$$

where $\bar{\mathbf{I}}_4$ is the 4 × 4 unit matrix, one obtains the following equations:

$$\begin{aligned} |S_{11}|^2 + |S_{12}|^2 + |S_{13}|^2 + |S_{14}|^2 &= 1, \\ S_{11}S_{12}^* + S_{12}S_{11}^* + S_{13}S_{14}^* + S_{14}S_{13}^* &= 0, \\ S_{11}S_{13}^* + S_{12}S_{14}^* + S_{13}S_{11}^* + S_{14}S_{12}^* &= 0, \\ S_{11}S_{14}^* + S_{12}S_{13}^* + S_{13}S_{12}^* + S_{14}S_{11}^* &= 0. \end{aligned} \tag{A5}$$

Using the system of equations (A5), it was shown in [26] that for an ideally matched four-port with $S_{11} = 0$, in the scattering matrix one of the elements S_{12}, S_{13}, or S_{14} must be

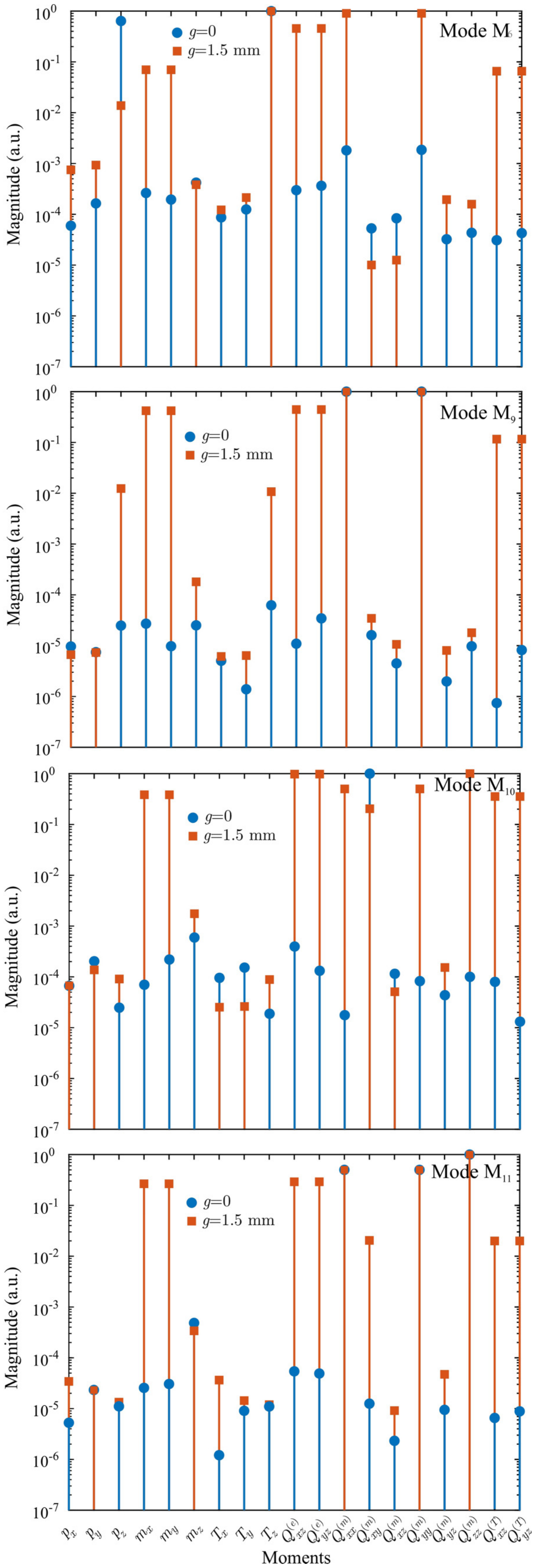

FIG. 8. Multipole expansion analysis for BIC modes M6 and M9–M11 calculated in both the symmetric and asymmetric metasurface case.

equal to 0. Inversely, if one of the ports is decoupled (i.e., $S_{12} = 0$, or $S_{13} = 0$, or $S_{14} = 0$), one gets $S_{11} = 0$, i.e., the matched structure.

The metasurface is polarization-dependent, and this can be demonstrated as follows. If the input wave is x-polarized, namely the input field is described by the vector $\mathbf{E}_{\text{in}} = (1, 0, 0, 0)^t$, the output field will be $\mathbf{E}_{\text{out}} = (S_{11}, S_{12}, S_{13}, S_{14})^t$. However, if the input wave is the y-polarized field vector $\mathbf{E}_{\text{in}} = (0, 1, 0, 0)^t$, the output is $\mathbf{E}_{\text{out}} = (S_{12}, S_{11}, S_{14}, S_{13})^t$, different from the previous case of x-polarized input. This analysis also demonstrates that due to symmetry, the metasurface possesses an interesting peculiarity. The amplitudes of the waves at the output ports 3 and 4 for the two orthogonal polarizations of the incident wave are interchanged.

If the input plane wave is linearly polarized at 45°, hence $\mathbf{E}_{\text{in}} = (1, 1, 0, 0)^t$, the output will be $\mathbf{E}_{\text{out}} = [(S_{11} + S_{12}), (S_{11} + S_{12}), (S_{13} + S_{14}), (S_{13} + S_{14})]^t$. In this case, the reflections at ports 1 and 2 are equal, and there is equal division of the output power between ports 3 and 4. Moreover, both the reflected and transmitted fields maintain the input linear diagonal polarization; no rotation is observed. We stress again that these properties are defined only by symmetry, and therefore they do not depend on the frequency. However, if the input wave is linearly polarized at −45° with $\mathbf{E}_{\text{in}} = (-1, 1, 0, 0)^t$, the output will be $\mathbf{E}_{\text{out}} = [(-S_{11} + S_{12}), (S_{11} - S_{12}), (-S_{13} + S_{14}), (S_{13} - S_{14})]^t$. Therefore, the response of the metasurface for linearly polarized waves at +45° and −45° is different, since unlike $x = y$, $x = -y$ is not a diagonal symmetry plane.

In the scenario of a square-slot resonator of the unit cell with four symmetrical bridges, the symmetry of the metasurface is increased to D_{4h}, thus allowing for one more element of symmetry to be included in the calculus. This can be C_{4z}, which corresponds to a rotation by $\pi/2$ around the z-axis. In that case, one gets $S_{12} = S_{14} = 0$ for the elements of the scattering matrix, and the metasurface response becomes polarization-independent and, hence, no polarization conversion can be observed.

APPENDIX B: WAVEGUIDE MEASUREMENT OF ZIRCONIA PERMITTIVITY

To characterize the dielectric properties of zirconia, a test slab with a cross section matching that of a WR-90 waveguide (22.86×10.16 mm^2) and a measured thickness of 3.08 mm was 3D-printed in the same batch and under the same conditions as the fabricated metasurface. The slab was placed inside an empty section of an WR-90 waveguide, which is then connected to the VNA ports as in the configuration shown in the inset of Fig. 7. A second waveguide section was added and sealed at the sample under test (SUT) ports. The ends of the resulting waveguide were connected via coaxial ports to a vector network analyzer (ANRITSU MS 37397D), which was calibrated by the Through-Reflect-Match technique.

The measured $|S_{21}|$ spectrum was compared to FEM-simulated spectra. The real part of the zirconia relative dielectric constant and the loss tangent were varied by 0.2 and 0.001, respectively. The combination providing the best-fitting result was found to be $\varepsilon_r = 32.8(1 - j0.003)$ and the agreement between the measured and calculated spectra is shown in Fig. 7. The shallow but sharp resonances in the measured spectrum were found to originate from small gaps (in the order of tens of μm), which were unavoidably introduced between the sample sides and the waveguide walls. Their presence, however, did not alter the overall shape of the transmission spectrum, which is accurately captured by the simulation.

The resulting value of $\varepsilon_r = 32.8(1 - j0.003)$ is consistent with the range of values reported in the literature for yttria-stabilized zirconia [10,15,27,28]. The same studies indicate that material dispersion in the considered frequency range is low, so this value was also considered for the metasurface studies around 20 GHz.

APPENDIX C: MULTIPOLE DECOMPOSITION OF RESONANT BIC MODES

Here, the results of the multipole expansion analysis for the modes M6 and M9–M11 of the metasurface are presented (Fig. 8). Similar to the case of M5, mode M6 exhibits magnetic field loops, which lead to a predominantly toroidal dipole T_z in the symmetric case. Modes M9–M11 are characterized by magnetic quadrupole field configurations, which correspond to the $Q^{(m)}_{xx}$, $Q^{(m)}_{yy}$ (mode M9), $Q^{(m)}_{xy}$ (mode M10), and $Q^{(m)}_{xx}$, $Q^{(m)}_{yy}$, $Q^{(m)}_{zz}$ (mode M11) moments. In all cases, symmetry breaking leads to the appearance of strong in-plane magnetic dipole and electric quadrupole Q^e_{yz}, Q^e_{xz} moments, thus transforming the BIC modes into qBIC ones.

[1] S. M. Kamali, E. Arbabi, A. Arbabi, and A. Faraon, Nanophotonics **7**, 1041 (2018).

[2] D. C. Zografopoulos and O. Tsilipakos, Mater. Adv. **4**, 11 (2023).

[3] Y. Hu, X. Wang, X. Luo, X. Ou, L. Li, Y. Chen, Y. Ping, S. Wang, and H. Duan, Nanophotonics **9**, 3755 (2020).

[4] A. S. Kupriianov, Y. Xu, A. Sayanskiy, V. Dmitriev, Y. S. Kivshar, and V. R. Tuz, Phys. Rev. Appl. **12**, 014024 (2019).

[5] D. R. Abujetas, Á. Barreda, F. Moreno, A. Litman, J.-M. Geffrin, and J. A. Sánchez-Gil, Laser Photon. Rev. **15**, 2000263 (2021).

[6] D. C. Zografopoulos, J. F. Algorri, A. Ferraro, B. García-Cámara, J. M. Sánchez-Pena, and R. Beccherelli, Sci. Rep. **9**, 7544 (2019).

[7] D. C. Zografopoulos, J. F. Algorri, W. Fuscaldo, J. M. López-Higuera, R. Vergaz, J. M. Sánchez-Pena, I.-A. Karolos, R. Beccherelli, V. E. Tsioukas, T. V. Yioultsis, and E. E. Kriezis, Adv. Opt. Mater. **9**, 2002143 (2021).

[8] O. Tsilipakos, A. C. Tasolamprou, T. Koschny, M. Kafesaki, E. N. Economou, and C. M. Soukoulis, Adv. Opt. Mater. **6**, 1800633 (2018).

[9] L. Li, J. Wang, M. Yan, M. Feng, and S. Qu, AIP Adv. **13**, 125022 (2023).

[10] T. Whittaker, S. Zhang, A. Powell, C. J. Stevens, J. Y. C. Vardaxoglou, and W. Whittow, IEEE Antennas Propag. Mag. **65**, 10 (2023).

[11] T. Q. van Hoang, M. Bertrand, E. Vandelle, and B. Loiseaux, in *2022 52nd European Microwave Conference (EuMC)* (IEEE, Piscataway, NJ, 2022), pp. 852–855.

[12] Y. Oh, V. Bharambe, B. Mummareddy, J. Martin, J. McKnight, M. A. Abraham, J. M. Walker, K. Rogers, B. Conner, P. Cortes, E. MacDonald, and J. J. Adams, Addit. Manuf. **27**, 586 (2019).

[13] F. Ferrero, T. Nguyen, T. L. Huy, J. Source, R. Faye, and G. de Calan, in *2022 16th European Conference on Antennas and Propagation (EuCAP)* (2022), pp. 1–3.

[14] S. Wang, L. Zhu, Y. Li, G. Zhang, J. Yang, J. Wang, and W. Wu, IEEE Antennas Wirel. Propag. Lett. **19**, 350 (2020).

[15] C. D. Morales, C. Morlaas, A. Chabory, R. Pascaud, M. Grzeskowiak, and G. Mazingue, Electron. Lett. **57**, 679 (2021).

[16] C. R. Mejias-Morillo, J. B. Shivakumar, S. L. Yu, B. Roberts, P. Cortes, E. Macdonald, A. V. Polotai, and E. A. Rojas-Nastrucci, IEEE Open J. Antennas Propag. **3**, 1289 (2022).

[17] J. F. Algorri, F. Dell'Olio, P. Roldán-Varona, L. Rodríguez-Cobo, J. M. López-Higuera, J. M. Sánchez-Pena, V. Dmitriev, and D. C. Zografopoulos, Opt. Express **30**, 4615 (2022).

[18] J. F. Algorri, F. Dell'Olio, Y. Ding, F. Labbé, V. Dmitriev, J. M. López-Higuera, J. Sánchez-Pena, L. Andreani, M. Galli, and D. Zografopoulos, Opt. Laser Technol. **161**, 109199 (2023).

[19] O. Tsilipakos, L. Maiolo, F. Maita, R. Beccherelli, M. Kafesaki, E. E. Kriezis, T. V. Yioultsis, and D. C. Zografopoulos, Appl. Phys. Lett. **119**, 231601 (2021).

[20] V. Savinov, V. A. Fedotov, and N. I. Zheludev, Phys. Rev. B **89**, 205112 (2014).

[21] I. L. d. Camargo, J. R. Verza, J. Garcia, D. Di Federico, C. A. Fortulan, and A. P. da Luz, Mater. Lett. **355**, 135510 (2024).

[22] X. Fu, B. Zou, H. Xing, L. Li, Y. Li, and X. Wang, Ceram. Int. **45**, 17630 (2019).

[23] H. Xing, B. Zou, S. Li, and X. Fu, Ceram. Int. **43**, 16340 (2017).

[24] S. Zhong, Q. Shi, Y. Deng, Y. Sun, C. Politis, and S. Yang, Ceram. Int. **48**, 33485 (2022).

[25] V. Dmitriev, IEEE Trans. Antennas Propag. **61**, 185 (2013).

[26] J. L. Altman, *Microwave Circuits* (Van Nostrand, New Jersey, USA, 1984).

[27] M. Lanagan, J. Yamamoto, A. Bhalla, and S. Sankar, Mater. Lett. **7**, 437 (1989).

[28] N. Delhote, D. Baillargeat, S. Verdeyme, C. Delage, and C. Chaput, IEEE Trans. Microw. Theor. Techn. **55**, 548 (2007).